The Bidirectional Effects of AVHRR Measurements over Boreal Regions

Zhanqing Li, Josef Cihlar, Xingnian Zheng, Louis Moreau, and Hung Ly

Abstract— **The objectives of this paper are to analyze the bidirectional effects of satellite data over six land-cover types in northern regions, and to test a method for the routine correction of these effects. Analyses and corrections were carried out with both single-day and 10-day composite data obtained by the advanced very high resolution radiometer (AVHRR) from central Canada acquired in 1993/1994, in part, for the boreal ecosystem and atmosphere study (BOREAS). The model of Wu *et al.* [21], developed from a separate data set collected at lower latitudes, was employed for correcting the effects. The analysis showed a strong viewing angle dependence in AVHRR channels 1 and 2 from both single-day images and composites. Reflectances at extreme viewing angles are two to four times larger than those observed near nadir. On average, the effects introduce a variation of 30% relative to mean reflectances. Although the effects decrease in the normalized difference vegetation index (NDVI), they are nevertheless significant before the correction. Using the model of Wu *et al.* [21], the BRDF-related variability is reduced by about 68% in channel 1 and 71% in channel 2. After a simple adjustment of the model coefficients, a further reduction of 4% (channel 1) and 6% (channel 2) of the BRDF-related variability was achieved for the 10^6 km^2 BOREAS region. The effectiveness of the correction with both original and refined model of Wu *et al.* was found to be weakly dependent on land-cover type. Corrections for coniferous, mixed wood, and cropland are better than other land-cover types (rangelands/pasture, deciduous, and transitional forests) with residual BRDF errors around 0.05 in both channels. Overall, the model (albeit simple) performs reasonably well throughout the growing season. To apply the model, only general knowledge of land-cover type is required, namely forest, cropland, grassland, and bare ground.**

I. Introduction

NORTHERN ecosystems play an important role in regional and global weather and climate. A recent analysis [1] suggested that the Boreal Forest, a major biome of the northern ecosystem, determines the position of the arctic front along its northern edge, and thus, has an essential role in defining high-latitude weather and climate. Interactions between northern vegetation and global climate involve complex feedbacks between atmosphere, terrestrial surface, Arctic Ocean, and sea ice/snow [2]. As a result, boreal climate and ecosystems are particularly vulnerable to global changes. Increasing CO_2 has an amplified warming effect at high latitudes (45°N–65°N) [3], whereas boreal deforestation could lower temperature by up to 10° and lead to irreversible disappearance of the forest [2]. Studies repeatedly suggest that boreal biomes are large terrestrial sinks of CO_2 [4]–[6]. Northern ecosystems have thus become an important theme of global change studies. An example is the boreal ecosystem-atmosphere study (BOREAS) [7]. BOREAS is an international, interdisciplinary, scientific program whose overall goal is to understand the interactions between the atmosphere and boreal forests through the exchange of heat, energy, and gases, particularly H_2O, CO_2, and CH_4. Over large spatial scales, remote sensing is the only feasible and economical means of monitoring the state variables that control the exchange of these quantities. Therefore, large amounts of remote-sensing data were acquired during the BOREAS campaigns for retrieving surface fluxes, driving and testing models, and studying the processes governing surface-atmosphere interactions.

Measurements from the advanced very high resolution radiometer (AVHRR) are among the most useful satellite data for land monitoring [8]. Many terrestrial parameters essential for BOREAS can be derived from AVHRR [9] such as land cover type [10]–[11], photosynthetically active radiation [12]–[14], leaf-area index [9], and CO_2 flux [15]. To derive these parameters from AVHRR measurements reliably and consistently necessitates several preprocessing steps: radiometric calibration, geo-referencing, angular correction, removal of atmospheric and cloud effects, etc. [16]. This study addresses one of these steps, namely, the angular correction of the AVHRR observations made over several predominant northern land-cover types under clear-sky conditions.

The angular correction aims at removing the dependence of AVHRR measurements on sun-target-sensor geometry. Mathematically, the dependence is expressed as a bidirectional reflectance distribution function (BRDF). The bidirectional effect is one of the classical issues in remote sensing studies. Just like the spectral dependence, the angular dependence provides new information about the properties of the sensed target [17]. However, for many geophysical and biogeochemical remote-sensing applications, the effect is often treated as an inherent problem associated with the use of a scanning radiometer, especially if insufficient measurements are available to characterize the BRDF. After many years of study, it is still one of the most uncertain steps in the processing of remote sensing data [18]. This is partially due to the technical difficulties in obtaining simultaneous measurements from multiple angles, and partially to its strong variability with many factors.

Manuscript received December 4, 1995; revised April 24, 1996. The work of X. Zheng was supported by the Chinese Academy of Sciences while he was visiting CCRS.

Z. Li and J. Cihlar are with the Canada Centre for Remote Sensing, Ottawa, ON, K1A 0Y7 Canada.

X. Zheng is with the Institute of Remote Sensing Applications, Academia Sinica, P.R. China.

L. Moreau and H. Ly are with Intera Information Technologies Ltd., Ottawa, Canada.

Publisher Item Identifier S 0196-2892(96)06806-4.

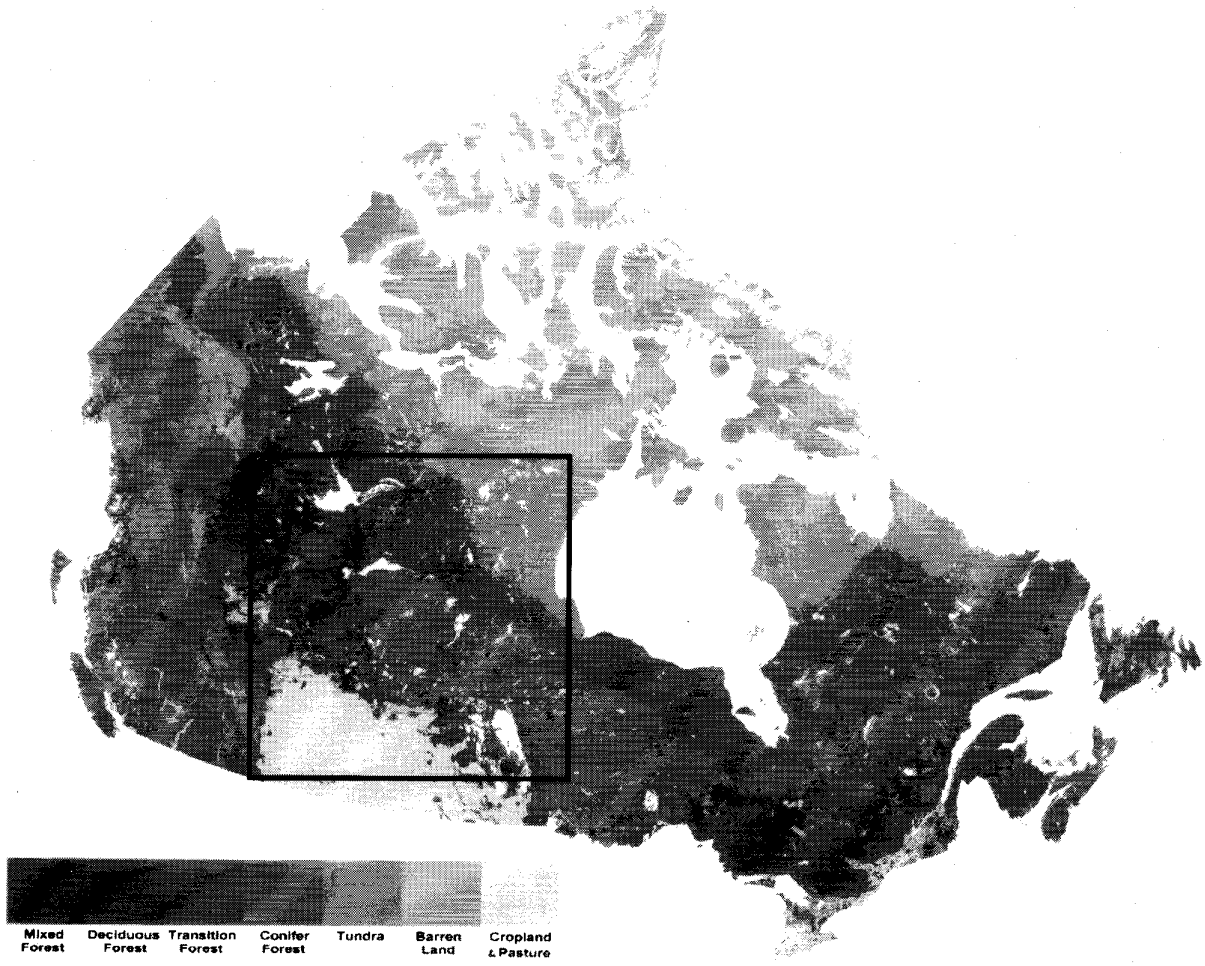

Fig. 1. Land-cover map of Canada derived from AVHRR images. The square delineates the study area of 1500 × 1500 km^2 over part of Saskatchewan, Manitoba, Alberta, and northwest territories of Canada.

Bidirectional effects in AVHRR measurements have been addressed in previous studies [19]–[22]. The objectives of this study are to 1) document and analyze the bidirectional effects of clear-sky AVHRR measurements made over different types of northern biomes, 2) test and improve the performance of the BRDF model of Wu *et al.* [21] with an independent data set, and 3) provide a corrected comprehensive remote-sensing product for use in the BOREAS project. In addition, the results of the study will assist in selecting a BRDF model for operational processing of clear-sky AVHRR measurements in northern regions. The data and model used are introduced in Sections II and III, respectively. Analysis and correction of the bidirectional effect is presented in Section IV. Section V concludes the study.

II. Data Processing

AVHRR has five spectral bands in the visible (channel 1), near-infrared (channel 2), mid-infrared (channel 3), and thermal infrared (channels 4 and 5) regions of the electromagnetic spectrum. Only the two shortwave channels (1 and 2) which have been used extensively for terrestrial monitoring are dealt with in this study. The AVHRR is onboard the National Oceanographic and Atmospheric Administration's (NOAA) polar-orbiting sun-synchronous satellites. Typically, there are two polar-orbiting NOAA satellites operated concurrently with different overpass time: one in the morning and another in the afternoon during the daytime. Scenes at low latitudes are viewed only once a day by one satellite, while multiple observations from different viewing angles are available at high latitudes owing to the convergence of satellite orbits. AVHRR scans the earth in a cross-track mode with a maximum scan angle of 55.4°. The field of view degrades from a circle with a 1.1 km diameter at nadir to an ellipse (2.5 km × 6.8 km in size) at the largest scanning angle.

AVHRR data employed in this study were obtained from NOAA 11, an afternoon spacecraft, over an area of 1500 × 1500 km^2 that covers part of Manitoba, Saskatchewan, Alberta, and northwest territories of Canada (Fig. 1). It encompasses the BOREAS region of 1000 × 1000 km^2. We intentionally chose a larger area to include a wider range of land-cover types and conditions. The land-cover map of Canada shown in Fig. 1 was derived from AVHRR images

[23]. It has eight cover types including mixed forest, deciduous forest, transition forest, conifer forest, tundra, barren, cropland, and pasture. The map has a nominal resolution of 1 km, but the actual resolution may be significantly coarser due to the larger AVHRR footprints at larger viewing angles. Therefore, the distribution represents regional trends better than local detail. The selected region contains all types of land cover across Canada distinguished by the classification, but does not include the large topographic effects typical of the Rocky Mountains.

Two types of AVHRR data were employed: single-day images and ten-day composites. The raw HRPT data covering nearly the entire Canada landmass were obtained at a satellite receiving station of the Canada Centre for Remote Sensing (CCRS), Prince Albert, Saskatchewan. Data were processed using the GEOcoding and COMPositing (GEOCOMP) system [24] developed by CCRS and operated by the Manitoba Remote Sensing Centre. It performs sensor calibration, registration, and compositing of scenes which are selected within the full sensor swath. Radiance data from channels 1 and 2 were calibrated using post-launch time-dependent gain and offset coefficients [25]. Data registration was done with reference to ground control points obtained from high-resolution image chips, and the images were resampled using a modified Kaiser 16-point $\sin(x)/x$ kernel. To obtain a single-date image covering the entire study area, we need to mosaic several scenes together.

Clear-sky composites across the entire Canada landmass were produced for each ten-day period by retaining the measurements with the largest normalized difference vegetation index (NDVI) at the top of the atmosphere (TOA) [16]. NDVI is defined as the ratio of the difference over the sum of the reflectance in channel 2 and channel 1. Ten parameters were saved including five AVHRR channels, NDVI, three geometric angles (solar zenith, view zenith, and relative azimuth), and the date of acquisition. Although the composites are nominally cloud-free, they may, in fact, contain completely or partially cloud-contaminated pixels if these are least cloudy during the compositing period. Apart from clouds, the data can also be contaminated by smoke or other heavy aerosols, snow, and ice. These contaminated pixels were identified and eliminated from further analysis using information on the seasonal trends of albedo and NDVI [26]. All data employed in this study are at the TOA. No atmospheric correction was made. The methodology and qualitative conclusions regarding the bidirectional dependence are, however, also applicable to surface reflectance obtained after an atmospheric correction [16].

III. Bidirectional Reflectance Distribution Function (BRDF)

Bidirectional correction assumes knowledge of the BRDF. There have existed many BRDF's derived from observations and simulations [27]. They can be classified as empirical, physical, and semi-empirical. Empirical models have two formats, tabulation, and function. Tabulated BRDF's are obtained by sorting reflectance measurements into different viewing bins and then integrating all bin-mean reflectances over the entire viewing domain [28], [29]. Empirical models in the functional format can be obtained by fitting functions to observed reflectances with viewing angles as the arguments of the function [30]. Since most operational satellites do not provide measurements from all directions, it is often difficult to develop a BRDF solely based on satellite data. Besides, a model developed from a specific data set may be invalid for other data sets.

In contrast, physical models entail no observations as they are built on the physics of scattering process [31]–[34]. Unfortunately, due to the complex nature of the scattering problem, development of such models always necessitates certain assumptions that highly limit their utility. Furthermore, many model parameters are not readily available, such as leaf-angle distribution. Thus, semi-empirical models were constructed on the basis of the physics of radiative transfer with model coefficients to be tuned according to observations. Models in the form of linear combinations of a few basic functions called kernels are becoming increasingly popular, especially for the applications of land remote sensing [35]–[37]. From a mathematical point of view, a kernel-based BRDF is more effective if the kernels are orthogonal to each other, i.e., the integration of the product between two kernels over the viewing domain is equal to zero. Unfortunately, this constraint may not hold as the kernels are usually derived from the simplification of more complex physical models [38]. As a result, models of a small number of kernels can fit well certain types of observed angular patterns, but not necessarily work well for others. Nevertheless, kernel-driven models have many advantages over both empirical and physical models. From the operational and computational viewpoints, the most notable advantage is that they can be realized without having measurements across the entire viewing domain and yet be efficiently invertible. They can be versatile if different types of kernels are used to cope with different scattering processes, a strategy to be used in the processing of MODIS data from the earth observation system [39].

This study is based on a semi-empirical model of kernel-driven type that was developed by Wu *et al.* [21] with two kernels derived by Roujean *et al.* [35]. The model is given by

$$\rho_j(\theta_s,\theta_v,\phi) = K_0 + K_1 f_1(\theta_s,\theta_v,\phi) + K_2 f_2(\theta_s,\theta_v,\phi) \quad (1)$$

where ρ_j denotes reflectance in channel j $(j = 1,2)$. f_1 and f_2 are two kernels that depend on three angles, namely, solar zenith θ_s, view zenith θ_v, and relative azimuth ϕ (the difference between the solar azimuth and the sensor azimuth)

$$\begin{aligned} f_1(\theta_s,\theta_v,\phi) = {} & \frac{1}{2\pi}[(\pi-\phi)\cos\phi + \sin\phi]\tan\theta_s\tan\theta_v \\ & - \frac{1}{\pi}(\tan\theta_s + \tan\theta_v \\ & + \sqrt{\tan^2\theta_s + \tan^2\theta_v - 2\tan\theta_s\tan\theta_v\cos\phi}) \end{aligned} \quad (2)$$

$$\begin{aligned} f_2(\theta_s,\theta_v,\phi) = {} & \frac{4}{3\pi(\cos\theta_s + \cos\theta_v)} \\ & \cdot \left[\left(\frac{\pi}{2} - \xi\right)\cos\xi + \sin\xi\right] - \frac{1}{3}\Big] \end{aligned} \quad (3)$$

$$\cos\xi = \cos\theta_s\cos\theta_v + \sin\theta_s\sin\theta_v\cos\phi. \quad (4)$$

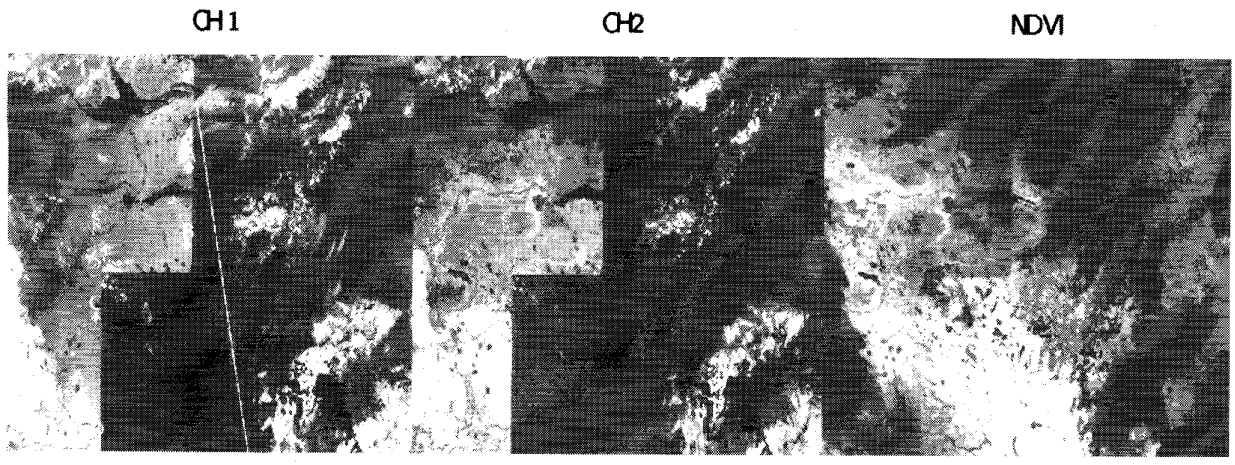

Fig. 2. AVHRR images of reflectance in channels 1 and 2 and NDVI on July 11, 1994 from NOAA-11 over the study area. The white line denotes the footprint of nadir view, to the left and right of which (on the right scene) are forward and back scattering, respectively. The entire left scene correspond to backscattering direction with extreme view zenith angles (>37°).

TABLE I
COEFFICIENTS OF THE BRDF'S DEVELOPED FOR AVHRR MEASUREMENTS AT CHANNELS 1 AND 2 OVER LAND SURFACES UNDER CLEAR CONDITIONS (FROM WU *ET AL.* [21])

Channel 1	a_{11}	a_{21}
barren	0.210	1.629
cropland	0.0	$3.622\text{NDVI}^{0.539}$
forest	0.0	$3.347\text{NDVI}^{0.153}$
grassland	$1.335e^{-11.39\text{NDVI}}$	$-0.493 + 14.94\text{NDVI} - 18.32\text{NDVI}^2$

Channel 2	a_{12}	a_{22}
barren	0.212	1.512
cropland	0.0	$1.620\text{NDVI}^{0.109}$
forest	0.0	$1.830\text{NDVI}^{-0.105}$
grassland	$7.745e^{-22.80\text{NDVI}}$	$-0.250 + 13.88\text{NDVI} - 20.43\text{NDVI}^2$

f_1 describes the bidirectional dependence for diffuse reflection from opaque reflectors on the ground and the shadowing effects of leaves. f_2 accounts for the contribution of volume scattering by a collection of randomly dispersed facets of canopies and bare soils. While these kernels were originally designed for dealing with surface BRDF, it was shown in [21] to be valid for TOA BRDF as well. The contribution of the atmosphere on TOA BRDF is tackled by f_2. K_0 represents the bidirectional reflectance for $\theta_s = \theta_v = 0$. K_1 and K_2 are coefficients denoting the relative contributions of f_1 and f_2. The values of the coefficients K_0, K_1 and K_2 were empirically determined for four land-cover types including barren, cropland, forest, and grassland using AVHRR measurements collected over 19 land sites located mostly in the U.S. and a few in Canada [21].

The BRDF model of Wu *et al.* [21] is given by

$$\Omega_j(\theta_s, \theta_v, \phi) = \frac{\rho_j(\theta_s, \theta_v, \phi)}{K_0} = 1 + a_{1j} f_1(\theta_s, \theta_v, \phi) + a_{2j} f_2(\theta_s, \theta_v, \phi) \quad (5)$$

where $a_{1j} = K_1/K_0$ and $a_{2j} = K_2/K_0$. They were fitted as functions of NDVI to account for the seasonal variation in the bidirectional effect (Table I). Using (5), one can normalize an AVHRR measurement made from a specific sun-target-satellite geometry denoted by $\rho_j(\theta_s, \theta_v, \phi)$ to any common geometry, e.g., the nadir view with a solar zenith of 45° [20]–[21]

$$\rho_j(45°, 0°, \phi) = \frac{\Omega_j(45°, 0°, \phi)}{\Omega_j(\theta_s, \theta_v, \phi)} \rho_j(\theta_s, \theta_v, \phi). \quad (6)$$

The normalized reflectance determined by (6) is particularly useful for monitoring purposes, since changes associated with differences in illumination and viewing geometry are removed or reduced. Of course, in principle, one could normalize reflectance measurments to other common viewing geometries, but the one used here may be preferable to many users. This is because the nadir view has the smallest atmospheric influence and 45° is the mean of minimum and maximum solar zenith angle. Another important application of the BRDF is that it can be used to determine an hemispheric albedo $A(\theta_s)$ from a reflectance observed from a single direction $\rho_j(\theta_s, \theta_v, \phi)$

$$A_j(\theta_s) = \frac{\rho_j(\theta_s, \theta_v, \phi)}{\pi \Omega_j(\theta_s, \theta_v, \phi)} \int_0^{2\pi} \int_0^{\pi/2} \Omega_j(\theta_s, \Theta_v, \Phi) \cdot \cos\Theta_v \sin\Theta_v \, d\Theta_v \, d\Phi. \quad (7)$$

IV. ANALYSIS

A. Single-Day Image

Fig. 2 presents a mosaic of AVHRR images for reflectance at channel 1, channel 2, and NDVI over the selected region on July 25, 1994. Except for a few scattered cumulus clouds, the images are mostly cloud free. The mosaic is composed of data from two consecutive passes separated by about 1.5 hours, the scene on the right being taken earlier. During this short period, clouds remained stationary, as indicated by the uninterrupted cloud pattern across the boundary between the two scenes. The bidirectional effect is evident from the striking contrast in brightness between left and right scenes, which is certainly not caused by natural variation. The abrupt changes in image brightness result from discontinuities in three geometric

angles. The difference in solar zenith plays a relatively small role as its variation (~15°) is smaller than those in viewing zenith (~25°) and relative azimuth (~180°). The right portion of the image has been acquired close to the nadir (view zenith of 0°) whose location is indicated by the white line on Fig. 2(a). Within this right portion of the image but to the right of nadir, view zenith increases from 0° to up to 50° (upper right corner) and relative azimuth angle is around 0°. Therefore, these pixels represent backscattering which increases with view zenith (whose magnitude is always less than the solar zenith, >65°). As a result, although reflectances are high, they are still considerably lower than the peak values that would occur when view zenith is equal to solar zenith and the relative azimuth is near 0°. This phenomenon is often referred to as "hot spot" that has been observed over most terrestrial scenes [21], [40]. The dark section of the right-hand portion of the image (between the scene junction and the nadir footprint) corresponds to forward scattering with relative azimuth close to 180° and viewing zenith ranging from 0° to 37°. The entire left portion of the scene represents backscattering with view zenith varying from 37° at upper left corner to 67° near the center of image. As the magnitude and trend of variation in view zenith are similar to those in solar zenith, the bright measurements displayed on the left scene echoes the effect of the hot spot. The bidirectional effect is also clearly manifest in the image of NDVI [Fig. 2(c)], although it is less pronounced than for reflectance. This is because BRDF for channel 1 reflectance is similar but unequal to that for channel 2 reflectance [21]. This confirms the need to correct NDVI measurements for view zenith effect, not just for solar zenith [8], [15].

The discontinuity across the scene junction is further quantified in Fig. 3. It depicts the changes in TOA reflectance (single pixel trace) in channels 1 and 2, NDVI, and three geometric angles along four short transects (35 km) across the scene junction (Fig. 2) with different types of land cover. The variation in viewing geometry is displayed along one transect, which is similar to other transects (Fig. 3). The contrast in reflectance between the forward- and backward-scattering directions is very large in both channels, the latter being two to four times brighter than the former. Over forests, channel 1 TOA reflectance increases from 0.06 in the forward scattering direction to around 0.2 in the backscattering direction. Reflectance in channel 2 is more variable. For transitional and coniferous forests, it ranges approximately from 0.1 to 0.4 from forward to backward-scattering directions in comparison to about 0.2–0.5 for deciduous forest. Over cropland, reflectance increases from 0.11 (0.20) to 0.32 (0.52) for channel 1 (2) from forward- to backward-scattering direction. Therefore, the largest distinction between clear and cloudy scenes occurs in channel 1 reflectance, measured in forward-scattering direction. In comparison to reflectance, NDVI displays a smaller and more gradual variation with viewing geometry (Fig. 3) larger in forward-scattering direction than in backward-scattering direction. The sharpest NDVI drop occurs over deciduous forest, decreasing from 0.60 to 0.43. The change in NDVI over conifers is even larger but takes place more gradually, owing to the steady decrease in

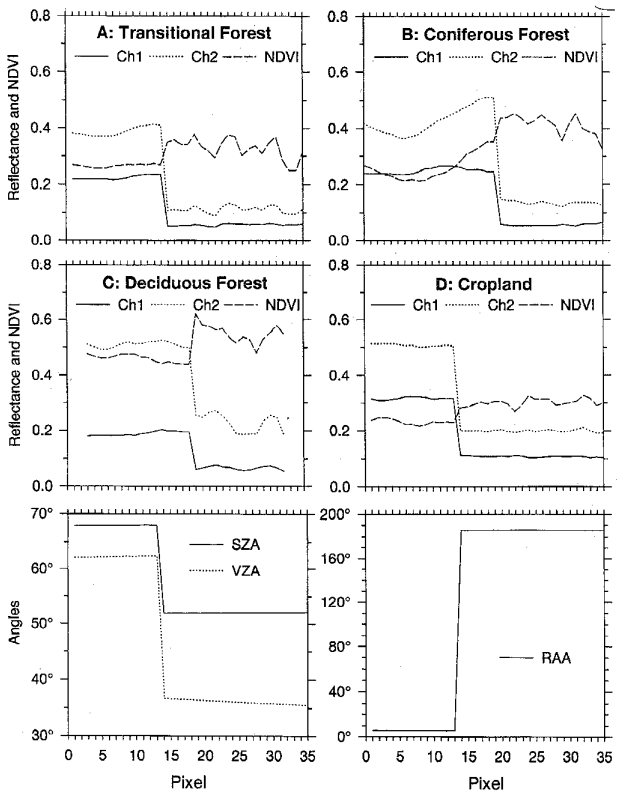

Fig. 3. Variations of reflectance and NDVI along the transects of four different biomes across the scene junction (c.f. Fig. 2). Changes in solar zenith, view zenith, and relative azimuth along one transect are plotted.

channel 2 reflectance. The smallest NDVI change is observed over cropland which is only about 0.05.

The bidirectional effects exhibited in Figs. 2 and 3 are strong enough to hinder our ability to monitor the changes of targets. The BRDF model of Wu *et al.* [21] was thus employed to normalize reflectances using (2)–(6). Fig. 4 presents the reflectances normalized to the solar zenith of 45° and viewing zenith of 0° for channels 1 and 2 and the NDVI. The contrast between the right and left scenes diminished significantly, but for reflectance it is not eliminated completely. In comparison, the correction appears sufficient to eliminate the discontinuity in the NDVI image. The reduction of the discontinuity is demonstrated more clearly in Fig. 5 which shows the same transects as in Fig. 3 but for data portrayed in Fig. 4. The only remaining weak discontinuity in NDVI is observed over deciduous forest. Reflectance in both channels shows small changes across the junction of two scenes, except for the deciduous forest where channel 2 discontinuity was removed completely. The remaining small discontinuity is not surprising given that the coefficients of the BRDF model employed here were derived empirically from a different data set [21].

B. Composite Data

Since the plane of sun-target satellite is very close to the principal plane of sun-target zenith, bidirectional effects in the composites are demonstrated in plots of reflectance against view zenith which was assigned to be negative for

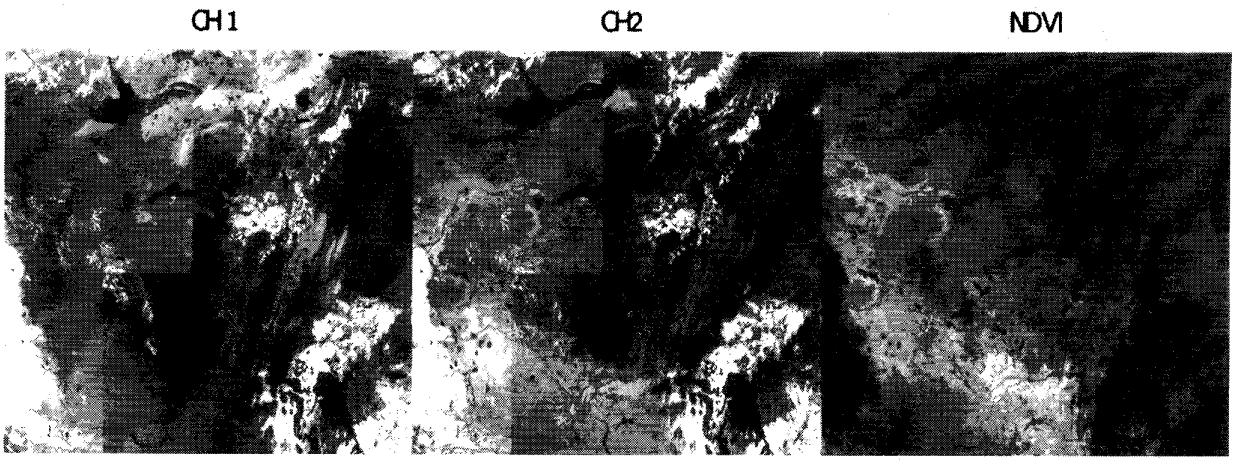

Fig. 4. Same as Fig. 2, but for normalized reflectance and the resulting NDVI.

backscattering (ϕ ~0°) and positive for forward scattering (ϕ ~180°). Fig. 6 presents clear-sky reflectance (contaminated pixels excluded) in channels 1 and 2 observed over six cover types of sufficient samples including mixedwood (coniferous/deciduous), deciduous, coniferous, and transitional forests, cropland, and rangland/pasture in the study region. As a result of natural variability the reflectances for the same cover type with the same viewing geometry fluctuate somewhat, especially for channel 2 reflectance whose variation amounts up to 0.2. Nevertheless, the trends in the variation of reflectance with viewing zenith are well defined. The trends for channel 1 reflectance are similar for all types of biomes, with minima occurring near the nadir and increasing with view zenith in both directions. Since surface reflectance in the channel 1 bandpass is very low for green vegetation, TOA reflectance is influenced more by atmospheric Rayleigh scattering which strengthens as view zenith increases. The surface bidirectional effect is, however, responsible for the weak asymmetric distribution with respect to nadir. Angular trends for channel 2 reflectance are distinct from those for channel 1. Overall, forward scattering is significantly weaker than backward scattering owing to the shadows cast by canopies. Angular trends for the four types of forest are similar but not identical. Reflectance variation over deciduous forest is more gradual than over coniferous forest, which may be associated with the clumping effect in conifer canopies [41]. For deciduous forest, reflectance shows an apparent local peak in the forward scattering direction at the viewing zenith angle of 43°. This angle is the same as solar zenith (see Fig. 7), and the enhanced reflection can thus be attributed to specular reflection. Weak specular reflection is visible over rangeland and pasture as well. While channel 2 reflection generally increases with view zenith in the backscattering direction, no hot spot is observed. This is because solar zenith is always larger than viewing zenith for backscattering, as shown in Fig. 7. Channel 2 reflectance is altered more by surface bidirectional effects as the atmospheric effect in channel 2 is relatively small. Hence, the angular patterns of channel 2 reflectance at the TOA are similar to those observed at the surface [40], [42].

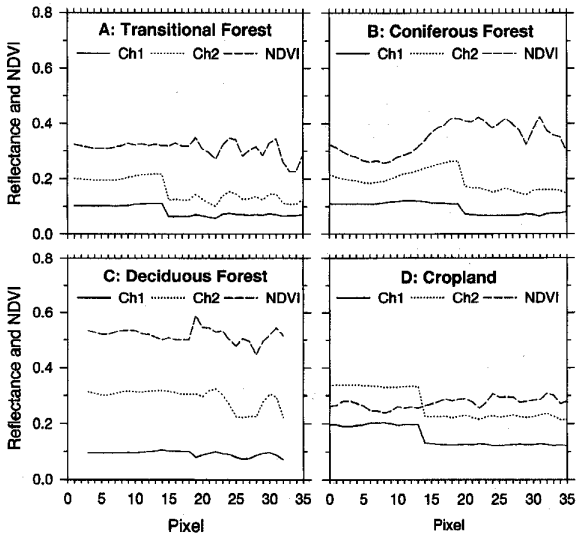

Fig. 5. Same as Fig. 3, but for normalized reflectance and the resulting NDVI.

Fig. 8 presents reflectances normalized to nadir view and a solar zenith of 45° by applying (1)–(6) to the data displayed in Fig. 6. Since the model of Wu *et al.* [21] has only four sets of coefficients (for cropland, grassland, forest, and barren land), reflectances observed over all types of forest were corrected using the same model. Despite this simplification, angular variations in TOA reflectances over these forests are reduced substantially. However, the specular reflection contribution remains essentially intact, most notably over deciduous forest as indicated by the small bump at a view zenith near 50°. This is not surprising since the kernels of Roujean *et al.* [35] do not take this effect into account. The correction would be somewhat better if BRDF's were derived and applied separately over different types of forest whose angular behaviors differ moderately, especially between deciduous and conifers. Indeed, we have used such an approach elsewhere [16]. The present BRDF model for forests is hybrid in that it was

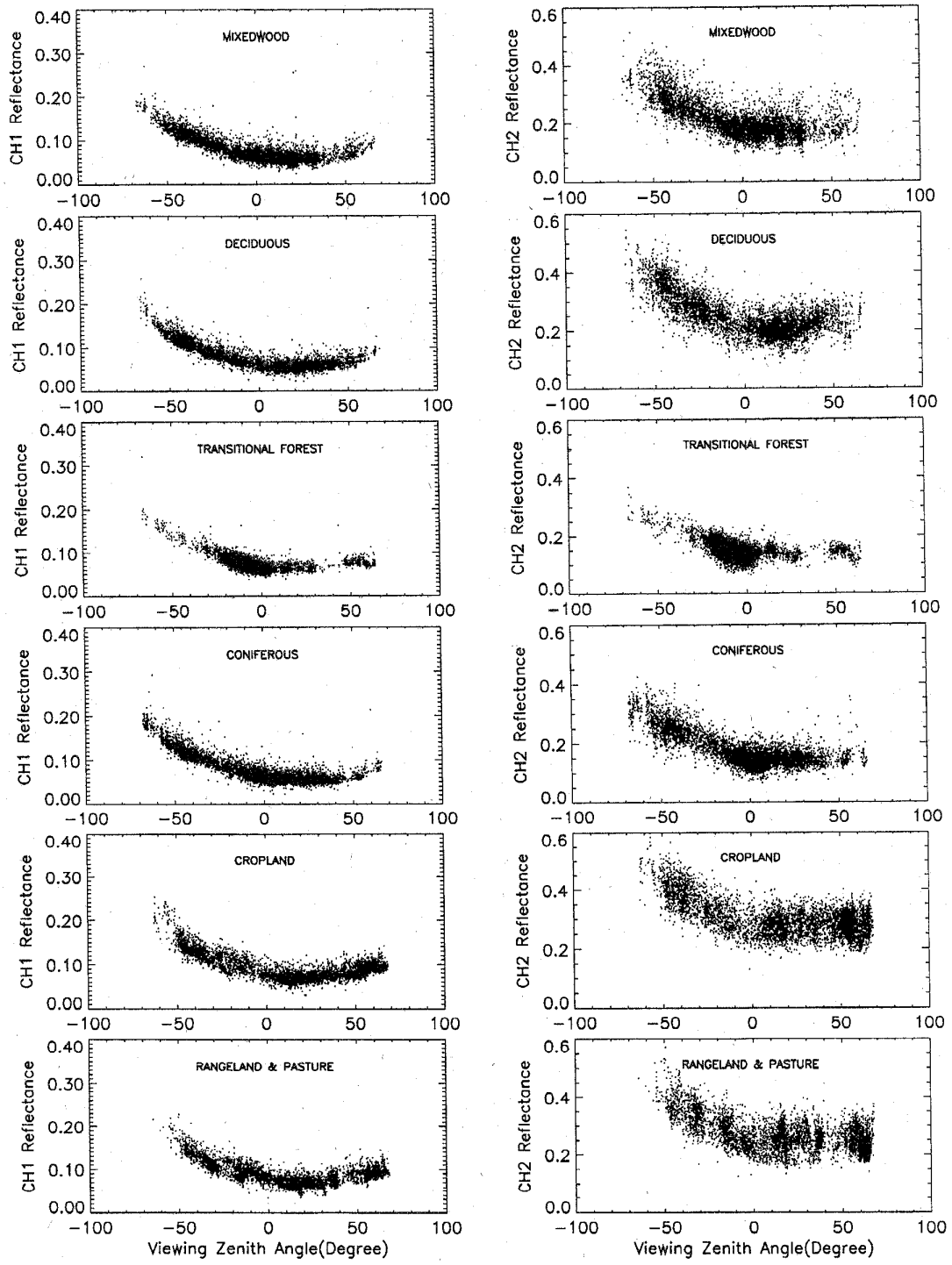

Fig. 6. Reflectance from AVHRR composite during the period July 21–30, 1993 over the study area against view zenith angle over six land-cover types. Positive and negative angles denote forward- and backward-scattering directions, respectively. Displayed are 5000 1-km pixels sampled randomly from the entire data sets for each land-cover type.

developed from measurements made over both deciduous and coniferous forests [21]. Imperfect correction stems also from the fact that surface and atmospheric conditions encountered in the development and application of the bidirectional models are not the same. This is probably the cause of the small, gradual increase in normalized reflectance toward backward scattering over cropland and rangeland/pasture to which grass model was applied. At any rate, the combined models are quite effective in reducing the angular variation of the reflectance measurements.

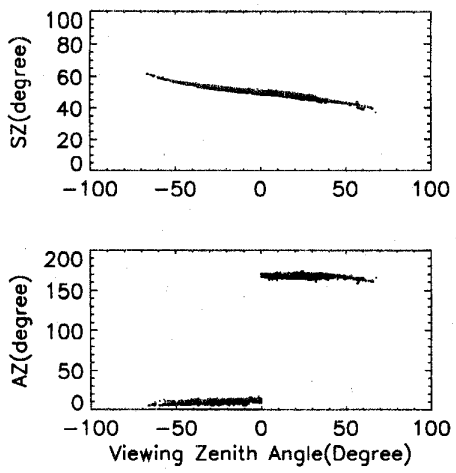

Fig. 7. Variations of solar zenith and relative azimuth with view zenith for the same period and region as in Fig. 6 over deciduous. Similar patterns of variations are observed over other land-cover types.

A bidirectional effect does not only affect reflectance, but also vegetation indices such as the NDVI. Fig. 9 shows the variations of NDVI derived from original (left panels) and normalized (right panels) reflectances in channels 1 and 2. The bidirectional effect is weaker for NDVI than for reflectance due to the similarity between channel 1 and channel 2. The maximum of NDVI change ranges from 0.1 to 0.2. After correction, trends in NDVI are barely visible for mixed-wood, deciduous, rangeland and pasture—and much weaker for conifer, transitional forest and cropland.

Since the bidirectional effect depends on sun angle and vegetation greenness [21], the angular trend of reflectance varies with season, as shown in Fig. 10. Instead of plotting reflectances as scatter points that would cause confusion between different months, Fig. 10 shows curves obtained by fitting the data with fourth-order polynomials for each month and land cover type, i.e.,

$$\rho(\theta_v) = a_0 + a_1\theta_v + a_2\theta_v^2 + a_3\theta_v^3 + a_4\theta_v^4. \tag{8}$$

Tests with the polynomials of different orders showed that (8) best preserves the angular trends displayed in scatter plots. The numbers associated with each curve in Fig. 10 quantifies the overall bidirectional effect. It is defined as

$$\delta\rho = \frac{\Delta\rho}{\overline{\rho}} \tag{9}$$

$$\overline{\rho} = \frac{1}{\theta_{\max} - \theta_{\min}} \int_{\theta_{\min}}^{\theta_{\max}} \rho(\theta_v)\, d(\theta_v) \tag{10}$$

$$\Delta\rho = \frac{1}{\theta_{\max} - \theta_{\min}} \int_{\theta_{\min}}^{\theta_{\max}} |\rho(\theta_v) - \overline{\rho}|\, d(\theta_v) \tag{11}$$

where $\theta_{\min}$ and $\theta_{\max}$ are the minimum and maximum of viewing zenith which are set to be $-65°$ and $65°$, respectively. $\Delta\rho$ and $\delta\rho$ denote, respectively, the overall absolute and relative BRDF effect as measured by the deviation of the fitted curve from a flat line. Note that the data used in Fig. 10 correspond to the last ten-day period in each month, not monthly mean. As indicated by both the curves and numbers, bidirectional effect depends on the spectral band, land cover, and month. It ranges from 0.17 to 0.39 and the mean of $\delta\rho$ is 0.31 for channel 1 and 0.24 for channel 2. For both channels, the bidirectional effect is strongest in September. The mean $\delta\rho$ over all types of biomes and for the two bands are equal to 0.27, 0.26, and 0.31 in May, July, and September, respectively. Solar zenith plays an essential role in modifying the bidirectional effect: the larger the solar zenith, the stronger the bidirectional effect is. It is thus more imperative to correct for this effect during early and late growing season than during the mid season, at least as far as the effect of the solar zenith angle is concerned. For the same reason, correction is more important at higher latitudes than at lower latitudes. It is seen from Fig. 10 that channel 1 reflectance over all forests except transitional forest is nearly independent of the season for viewing zenith less than 40°, but considerably higher in September than in July at large viewing angles. Seasonal variation of the bidirectional effect for channel 2 reflectance appears to be opposite to that of channel 1, i.e., more stable at large viewing zenith than at low-viewing zenith, except for transitional forest. The dependence of the bidirectional effect on season is slightly weaker for other cover types, but their reflectance value is very sensitive to season. In July, reflectance reaches minimum and maximum in channels 1 and 2, respectively, for cropland, rangeland, and pasture.

A novel feature of the model of Wu *et al.* [21] is the ability to account for the seasonal dependence of the bidirectional effect by using both solar zenith and NDVI as model inputs. This ability was tested with the same data as employed in Fig. 10. These data are independent of those used in the development of the model that were measured mostly over the U.S. [21]. Fig. 11 shows polynomial fits to reflectances normalized to the common geometry for individual pixels computed by the model of Wu *et al.* The values of $\delta\rho$ are computed as above using (9)–(11). Significant reduction in the bidirectional effect is illustrated clearly in the comparison of Figs. 10 and 11. The curves in Fig. 11 become much flatter and the values of $\delta\rho$ diminish. Most of the relative errors due to residual bidirectional effect decrease by a factor of three. The mean $\delta\rho$ over all cover types decreased from 0.31 to 0.10 (channel 1) and from 0.24 to 0.07 (channel 2). Besides, the dependence on season is lessened considerably, suggesting that a single model does a reasonable job in accounting for the bidirectional effect throughout the season. Residual variations of much smaller magnitude remain—exhibiting two patterns. One is the low-frequency global trends as observed over all cover types for channel 1, except transitional forest, and over cropland for channel 2. The other is the high-frequency local fluctuations as observed over the majority of land covers in channel 2.

In view of the complexity in defining the functions of a_{ij} against NDVI [21] and the fact that the original model of Wu *et al.* performs well throughout the season, a simple method of retuning the coefficients in [21] was adopted here. This

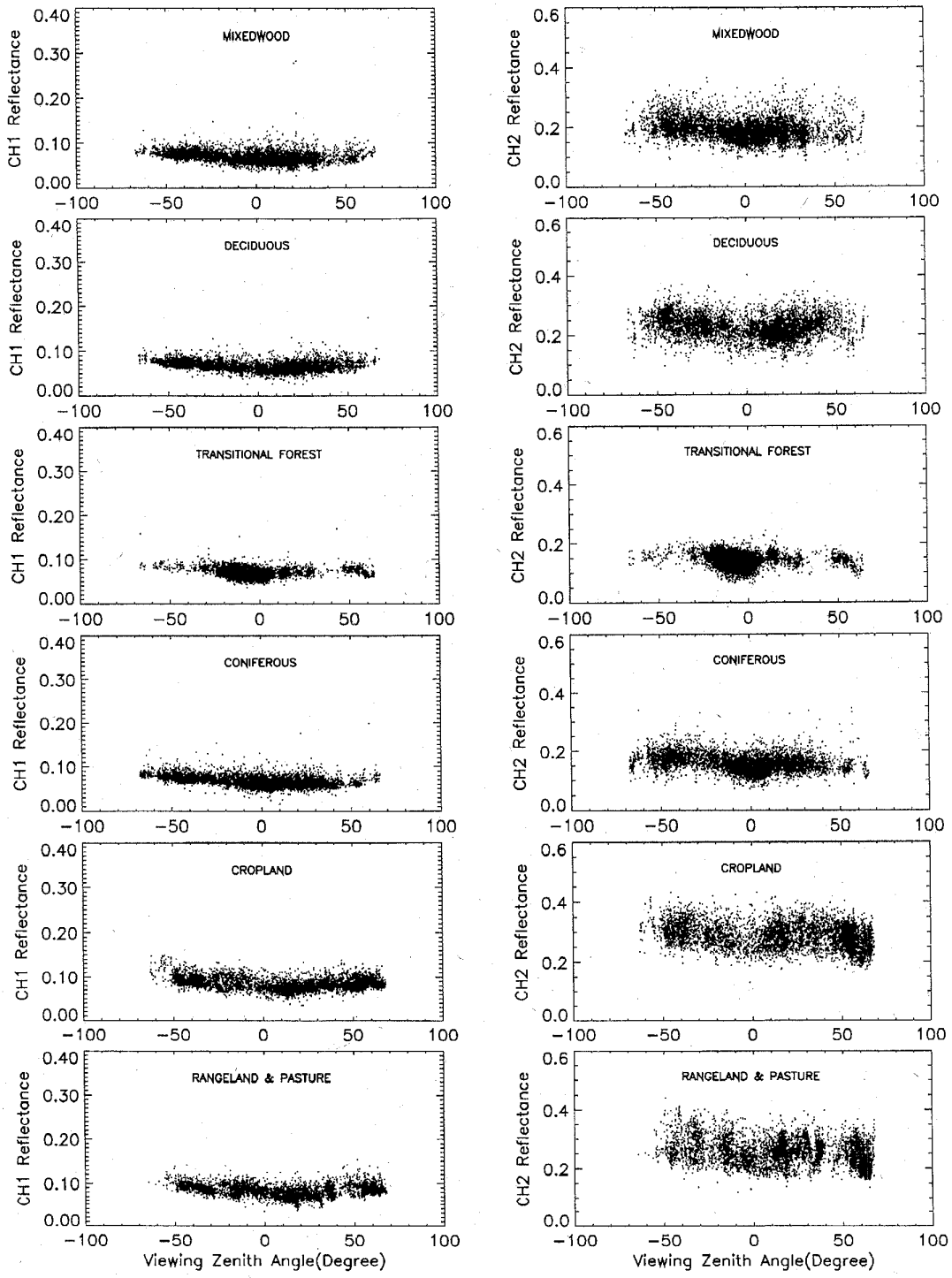

Fig. 8. Same as Fig. 6 but for reflectance normalized to a solar zenith angle of 45° and viewing zenith of 0° using the model of Wu *et al.* [21].

approach retains the same relationship of a_{ij} to NDVI by selecting new coefficients a'_{ij} to be proportional to the old ones, i.e.,

$$a'_{ij} = c_{ij} a_{ij} \tag{12}$$

c_{ij} was determined by fitting the satellite data of interest to the following regression equation:

$$\rho_j(\theta_s, \theta_v, \phi) = k_{0j} + k_{1j} a_{1j} f_1(\theta_s, \theta_v, \phi) + k_{2j} a_{2j} f_2(\theta_s, \theta_v, \phi) \tag{13}$$

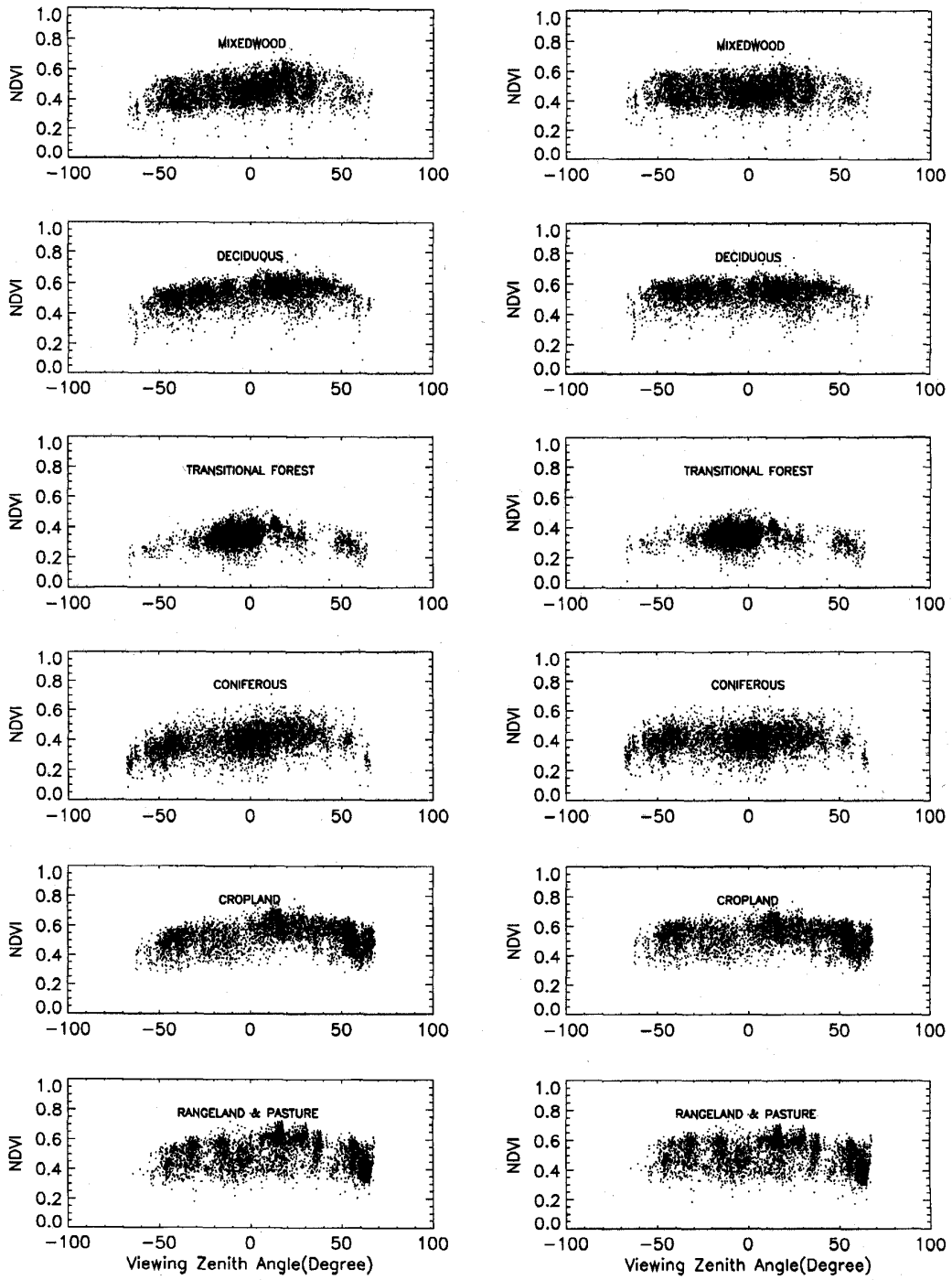

Fig. 9. Variations of NDVI derived from original (without bidirectional correction) and normalized reflectances (with bidirectional correction) in channels 1 and 2 with viewing zenith for the same data as those used in Figs. 6 and 8.

where a_{ij} are given in Wu *et al.* [21]. It follows from the comparison of (5) and (13)

$$c_{ij} = \frac{k_{ij}}{k_{0j}}. \tag{14}$$

Note that we intentionally use small "k" in (13) in lieu of capital "K" in (5) to differentiate the difference. The values of c_{ij} (Table II) were determined from the AVHRR composite images over the study region prepared at ten-day intervals from April through September 1993. Use of these new coefficients leads to a new set of normalized reflectances. The polynomial fits of these data are presented in Fig. 12. Moderate improvement is achieved and the overall mean $\delta\rho$ becomes 0.08 and 0.05 for channels 1 and 2, respectively.

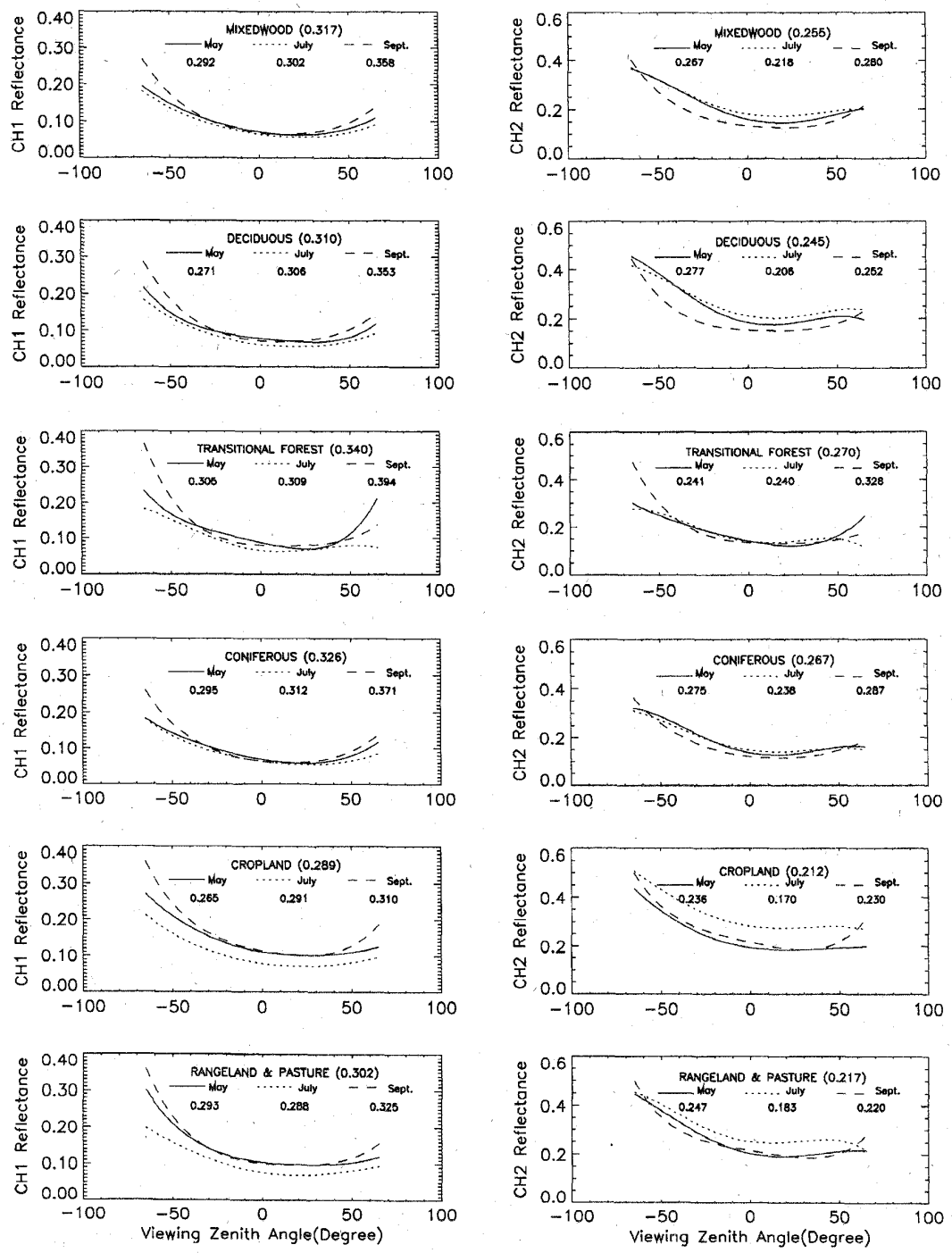

Fig. 10. Angular variations of reflectance with viewing zenith angle for the composites of the last ten-day period in May, July, and September 1994. The curves were obtained by fitting the original reflectances with four-order polynomials. The numbers represent the relative variations due to bidirectional dependence for each month and for three-month means (numbers in the paratheses).

For many remote-sensing applications, the uncertainties of such magnitudes should be acceptable, considering that errors introduced in other steps could be significantly larger, e.g., calibration, atmospheric correction, etc. It is clear from the comparison between Figs. 11 and 12 that the decrease in $\delta\rho$ is mainly due to the weakening of global residual variation while local fluctuations remains essentially intact. This is because the kernels of Roujean *et al.* do not account for the effects of hot spot and specular reflection, especially for channel 2 reflectance. In this regard, the kernels derived from Li–Strahler geometric-optical BRDF [38], [43] are expected to perform better.

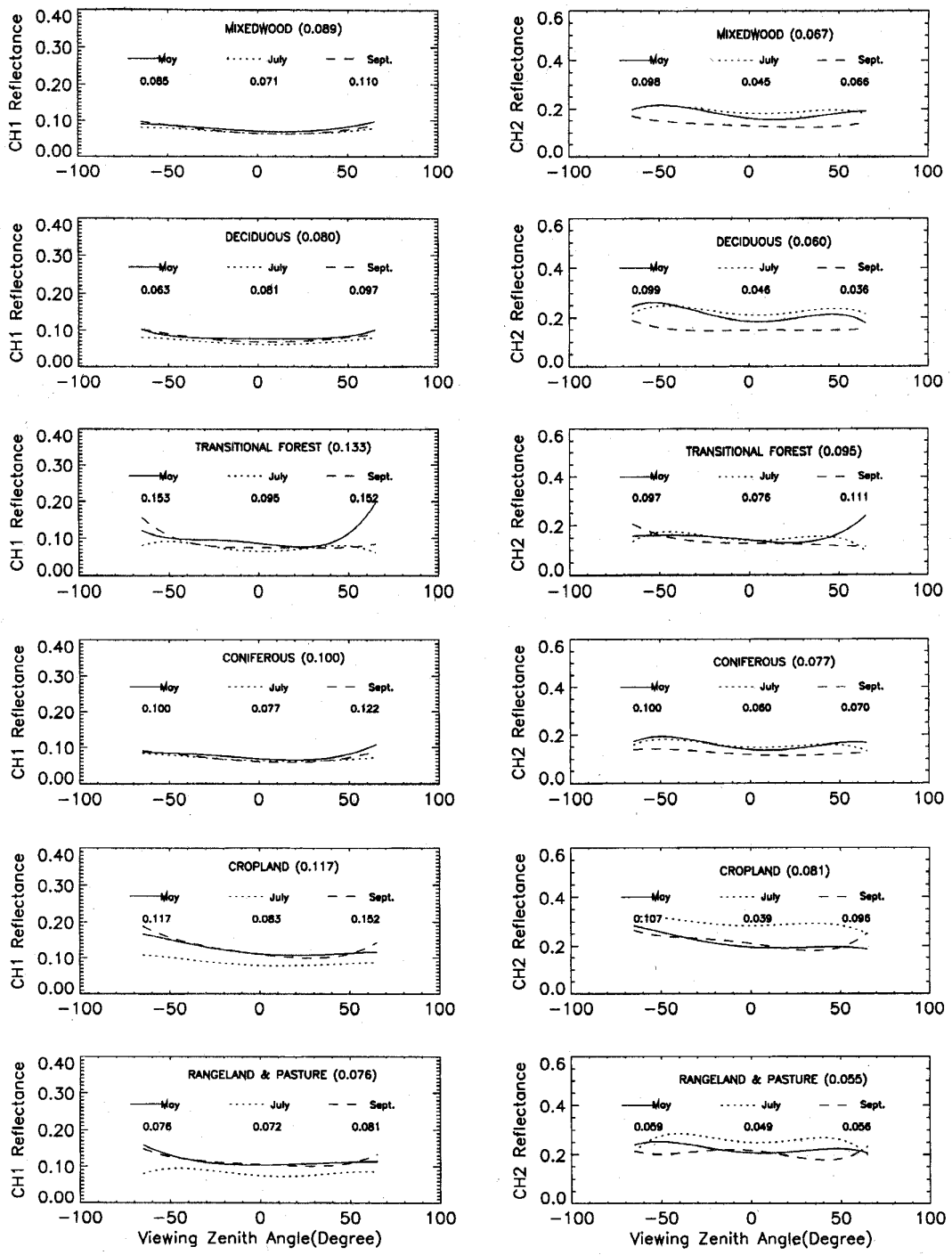

Fig. 11. Same as Fig. 10, but for reflectances normalized to nadir with a solar zenith of 45° using the model of Wu *et al.* [21].

V. Concluding Remarks

Bidirectional effect deals with the dependence of reflectance on sun-target-sensor geometry. For many geophysical applications, such an effect must be accounted for in the use of remote-sensing data based on BRDF's. This study first analyzed the bidirectional effect and then applied a BRDF model developed by Wu *et al.* [21] to the AVHRR data measured over a region of 1500 × 1500 km^2 in central-western Canada that encompasses the BOREAS study region. Six primary land-cover types in northern areas were studied including four forest types (deciduous, conifers, mixed wood, transitional forest, cropland, and rangeland/pasture). The study is limited to satellite measurements at the TOA, although the methodology and procedure are equally applicable to ground

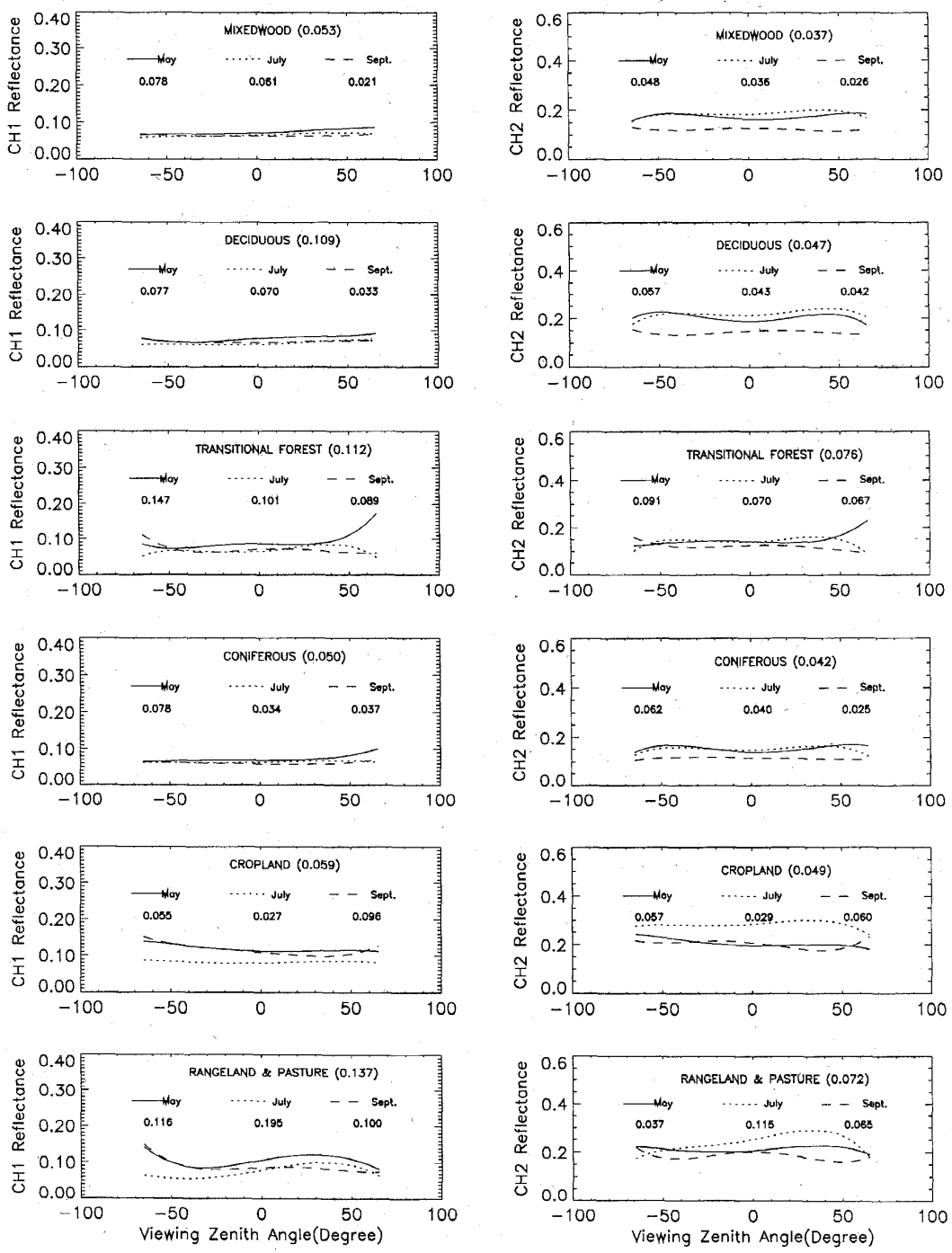

Fig. 12. Same as Fig. 11, but using the model of Wu *et al.* [21] with adjusted coefficients.

measurements obtained either from direct surface observations or from TOA reflectance measurements with atmospheric correction.

Two forms of AVHRR data were used in this study, single-day AVHRR images and clear-sky composites over ten-day periods. The bidirectional effect is clearly marked by the artificial discontinuity across the edge between two adjacent passes in single-day mosaic images. As a result of distinct viewing geometries, reflectance changes across the boundary by a factor of two to four, and NDVI differs by about 0.1. After bidirectional correction with the BRDF model of Wu *et al.* [21], changes in reflectance diminish radically but do not disappear completely and the discontinuity in NDVI vanishes. In the composite images, the effect is indicated by the strong

TABLE II
CORRECTION COEFFICIENTS (C_{IJ}) FOR THE MODIFIED MODEL OF WU *ET AL.* [21]

Channels	1		2	
Coefficients	c_{11}	c_{21}	c_{12}	c_{22}
Mixedwood forest	0.0	1.635	0.0	1.520
Deciduous forest	0.0	1.518	0.0	1.431
Conifer forest	0.0	1.853	0.0	1.580
Transitional forest	0.0	1.580	0.0	1.471
Cropland	0.0	1.520	0.0	1.474
Rangland/Pasture	-0.980	1.719	0.007	1.320

variation of reflectance with viewing zenith and azimuth angles. The strongest and weakest reflection is observed in the extreme backward-scattering direction and near the nadir, respectively. While such a gross pattern is common to all cover types under study, perceptible differences exist in the angular trends even among different types of forests. The trend is also subject to significant seasonal change with maximum and minimum occurring in the late and mid-season, respectively. The model of Wu *et al.* removes much of the trends from the composites throughout the season. The remaining dependence of reflectance on viewing geometry is partially associated with the limitation of the model kernels [35]. BRDF models composed of more candidate kernels could be more effective at the expenses of larger data base and more computation.

This study demonstrates that a routine correction of satellite data with a wide range of imaging geometries for bidirectional effects is feasible with relatively simple models such as Wu *et al.* [21]. While the model is land-cover dependent, comparatively few land-cover types need to be distinguished (four, in the present case). This information could be obtained readily from AVHRR data. In fact, substantially more detailed land-cover maps have been derived from AVHRR seasonal composites [11], and the global 1-km AVHRR project [8], [44] aims to produce similar maps for various parts of the world. With such land-cover data set, the model of Wu *et al.* [21] can also be adjusted, as demonstrated above, to better reflect regional characteristics of the BRDF response. This approach can be implemented for operational processing of AVHRR data [16].

The adequacy of the same methodology for other sensors will depend on the extent to which their spatial resolution and viewing geometry differ from those of AVHRR. This is principally due to the mixed land-cover types within larger pixels (which tend to reduce the magnitude of the bidirectional effect) and the sun-sensor orientation which may lead to the hot spot or specular reflection effects (these were present in our data only in a minor way). Although the differences in spectral bands may be significant, we feel that the AVHRR channels 1 and 2 already encompass most of the range of functional BRDF dependencies that are likely to be encountered for northern cover types at comparable spatial resolutions. For application in other areas, both differences in cover type and in spectral dependence of BRDF, in addition to spatial resolution and viewing geometry, should be taken into account.

ACKNOWLEDGMENT

The authors would like to thank J.-L. Roujean (CNRM/METEO, France) and A. Wu (University of British Columbia, Canada) for useful discussions, J. Chen (CCRS, Ottawa, ON, Canada) for reviewing the manuscript, F. Huang for helping generate computer graphics. They would also like to thank P. Hurlburt and colleagues at the Manitoba Remote Sensing Center in Winnipeg, Man., Canada, for GEOCOMP data processing.

REFERENCES

[1] R. A. Pielke and P. L. Vidale, "The boreal forest and the polar front," *J. Geophys. Res.*, vol. 100, pp. 25, 755-25, 758, 1995.
[2] G. B. Bonan, D. Pollard, and S. L. Thompson, "Effects of boreal forest vegetation on global climate," *Nature,* vol. 359, pp. 716–718, 1992.
[3] G. J. Boer, N. A. McFarlane, M. Lazare, "Greenhouse gas-induced climate change simulated with the CCC second generation general circulation model," *J. Climate,* vol. 5, pp 1045–1077, 1992.
[4] P. P. Tans, I. Y. Fung, and T. Takahashi, "Observational constraints on the global atmospheric CO_2 budget," *Sci.*, vol. 247, pp 1431–1438, 1990.
[5] P. Ciais, P. P. Tans, M. Trolier, J. W. C. White, R. J. Francey, "A large northern hemisphere terrestrial CO_2 sink indicated by the 13C/12C ratio of atmospheric CO_2," *Sci.*, vol. 269, pp 1098–1102, 1995.
[6] A. S. Denning, I. Y. Fung, and D. Randall, "Latitudinal gradient of atmospheric CO_2 due to seasonal change with land biota," *Nature,* vol. 376, pp. 240–243, 1995.
[7] P. Sellers, F. Hall, H. Margolis, B. Kelly, D. Baldocchi, G. den Hartog, J. Cihlar, M. G. Ryan, B. Goodison, P. Crill, K. J. Ranson, D. Lettenmaier, and D. E. Wickland, "The boreal ecosystem-atmosphere study (BOREAS): An overview and early results from 1994 field year," *Bulletin Amer. Meteor. Soc.*, vol. 76, pp. 1549–1577, 1995.
[8] J. R. G. Townshend, C. O. Justice, D. Skole, J.-P. Malingreau, J. Cihlar, P. Teillet, F. Sadowski, and S. Ruttenberg, "The 1 km resolution global data set: Needs of the International Geosphere Biosphere Programme," *Int. J. Remote Sensing,* vol. 15, pp. 3417–3441, 1994.
[9] P. J. Sellers, C. J. Tucker, G. J. Collatz, S. O. Los, C. O. Justice, D. A. Dazlich, and D. A. Randall, "A global 1° by 1° NDVI data set for climate studies. Part 2: The generation of global fields of terrestrial biophysical paramters from the NDVI," *Int. J. Remote Sensing* vol. 15, pp 3519–3545, 1994.
[10] S. W. Running, T. R. Loveland, L. L. Pierce, R. R. Nemani, and E. R. Hunt, Jr., "A remote sensing based vegetation classification logic for global land cover analysis," *Remote Sensing Environment*, vol. 51, pp 39–48, 1995.
[11] T. R. Loveland, J. W. Merchant, D. O. Ohlen, and J. F. Brown, "Development of a land cover characteristics database for the conterminous U.S," *Photograph. Eng. Remote Sensing*, vol. 57, pp 1453–1463, 1991.
[12] D. G. Dye and S. N. Goward, "Photosynthetically active radiation absorbed by global land vegetation in Aug. 1984," *Int. J. Remote Sensing*, vol. 14, pp. 3361–3364, 1993.
[13] Z. Li and L. Moreau, "A new approach for remote sensing of canopy absorbed photosynthetically active radiation—I: Total Surface Absorption," *Remote Sensing Environment* vol. 55, pp 175–191, 1996.
[14] L. Moreau and Z. Li, "A new approach for remote sensing of canopy absorbed photosynthetically active radiation—II: Proportion of canopy absorption," *Remote Sensing Environment*, vol. 55, pp 192–204, 1996.
[15] J. Cihlar, P. Caramori, R. Desjardins, P. Schuepp, and J. I. MacPherson, "Relationship between satellite-derived vegetation index and aircraft-based CO_2 measurements," *J. Geophys. Res.*, vol. 97, pp. 18 515–18 521, 1992.
[16] J. Cihlar, H. Ly, Z. Li, J. Chen, H. Pokrant, and F. Huang, "Multitemporal, multichannel AVHRR data sets for land biosphere studies: Artifacts and corrections," *Remote Sensing Environment*, to be published.
[17] B. Pinty and M. M. Verstraete, "Extracting information on surface properties from bidirectional reflectance measurements," *J. Geophys. Res.*, vol. 96, pp. 2865–2874, 1991.
[18] Z. Li, "On the angular correction of satellite data: The performance of ERBE angular dependence model in the Arctic," *Theory Applicat. Climatol.*, vol. 54, pp. 235–248, 1996.
[19] M. Leroy and J.-L. Roujean, "Sun and view angle corrections on reflectances derived from NOAA/AVHRR data," *IEEE Trans. Geosci. Remote Sensing*, vol. 32, pp. 684–697, 1994.
[20] G. Gutman, "Normalization of multi-annual global AVHRR reflectance data over land surfaces to common sun-target-sensor geometry," *Adv. Space Res.*, vol. 14, pp. 121–124, 1994.
[21] A. Wu, Z. Li, and J. Cihlar, "Effects of land cover type and greenness on advanced very high resolution radiometer bidirectional reflectances: Analysis and removal," *J. Geophys. Res.*, vol. 100, pp. 9179–9192, 1995.

[22] J. Cihlar, D. Manak, and N. Voisin, "AVHRR bidirectional reflectance effects and composite," *Remote Sensing Environment*, vol. 48, pp. 77–88, 1994.
[23] H. Pokrant, "Land cover map of Canada derived from AVHRR images," Manitoba Remote Sensing Ctr., Winnipeg, Manitoba, Canada.
[24] B. Robertson, A. Erickson, J. Friedel, B. Guindon, A. Sanz, T. Fisher, R. Brown, P. Teillet, M. D'Iorio, J. Cihlar, and A. Sancz, "GEOCOMP, a NOAA AVHRR geocoding and compositing system," in *Proc. ISPRS Conf. Commiss. 2*, Washington, DC, 1992, pp. 223–228.
[25] J. Cihlar and P. M. Teillet, "Forward piecewise linear model for quasireal time processing of AVHRR data," *Can. J. Remote Sensing*, vol. 21, pp. 22–27, 1995.
[26] J. Cihlar, "Identification of contaminated pixels in AVHRR composite images for studies of land biosphere," *Remote Sensing Environment*, to be published.
[27] A. H. Strahler, "Vegetation canopy reflectance modeling—Recent developments and remote sensing perspectives," in *Proc. 6th Int. Symp. Phys. Meas. Signature*, Val d'Isere, France, Jan. 17–21, 1994, pp. 593–600.
[28] J. T. Suttles, R. N. Green, P. Minnis, G. L. Smith, W. F. Staylor, B. A. Wielicki, I. J. Walker, D. F. Young, V. R. Taylor, L. L. Stowe, "Angular radiation models for Earth-atmosphere system: Vol. 1—Shortwave radiation," *NASA Ref. Publ.*, vol. 1184, pp. 114, 1988.
[29] V. R. Taylor and L. L. Stowe, "Reflectance characteristics of uniform earth and cloud surfaces derived from Nimbus-7 ERB," *J. Geophys. Res.*, vol. 89, pp. 4987–4996, 1984.
[30] C. L. Walthall, J. M. Norman, J. M. Welles, G. Campbell, and B. L. Blad, "Simple equation to approximate the bidirectional reflectance from vegetative canopies and bare soil surfaces," *Appl. Opt.* vol. 24, pp. 383–387, 1985.
[31] D. L. B. Jupp and A. H. Strahler, "A hotspot model for leaf canopies," *Remote Sensing Environment* vol. 38, pp. 193–210, 1991.
[32] B. Hapke, "Bidirectional reflectance spectroscopy, 1. Theory," *J. Geophys. Res.*, vol. 86, pp. 3039–3054, 1981.
[33] X. Li and A. H. Strahler, "Geometric-optical bidirectional reflectance modeling of a conifer forest canopy," *IEEE Trans. Geosci. Remote Sensing*, vol. GE-24, pp. 906–919, 1986.
[34] S. Liang, and A. H. Strahler, "Calculation of the angular radiance distribution for a coupled atmosphere and canopy," *IEEE Trans. Geosci. Remote Sensing*, vol. 31, pp. 491–502, 1993.
[35] J. L. Roujean, M. Leroy, and P. Y. Deschamps, "A bidirectional reflectance model of the earth's surface for the correction of remote sensing data," *J. Geophys. Res.*, vol. 97, pp. 20 455–20 468, 1992.
[36] W. Wanner, A. H. Strahler, J.-P. Muller, M. Barnsley, P. Lewis, X. Li, and C. L. Barker Schaaf, "Global mapping of bidirectional reflectance and albedo for the EOS MODIS project: The algorithm and the product," in *Proc. Int. Geosci. Remote Sensing Symp.*, Florence, Italy, July 10–14, 1995, pp. 525–529.
[37] P. Lewis, "The utility of kernel-driven BRDF model in global BRDF and albedo studies," *Proc. Int. Geosci. Remote Sensing Symp.*, Florence, Italy, July 10–14, 1995, pp. 1186–1188.
[38] W. Wanner, X. Li, and A. H. Strahler, "On the derivation of kernels for kernel-driven models of bidirectional reflectance," *J. Geophys. Res.*, vol. 100, pp. 21 077–21 089, 1995.
[39] A. Strahler, J.-P. Muller, M. J. Barnsley, R. d'Entremont, B. Hu, P. Lewis, X. Li, C. B. Schaaf, W. Wanner, B. Zhang, "MODIS BRDF/Albedo product: Algorithm theoretical basis document, Version 3.2," Boston Univ., MA, pp. 86, 1995.
[40] D. W. Deering, E. M. Middleton, and T. F. Eck, "Reflectance anisotropy for a spruce-hemlock forest canopy," *Remote Sensing Environment* vol. 47, pp. 242–260, 1994.
[41] J. M. Chen and J. Cihlar, "Retrieving leaf area index of boreal conifer forests using Landsat TM images," *Remote Sensing Environment*, vol. 55, pp. 153–162, 1996.
[42] E. M. Middleton, "Quantifying reflectance anisotropy of photosynthetically active radiation in grasslands," *J. Geophys. Res.*, vol. 97, pp. 18 935–18 946, 1992.
[43] X. Li and A. H. Strahler, "Geometric-optical bidirectional reflectance modeling of the discretecrown vegetation canopy: Effect of crown shape and mutual shadowing," *IEEE Trans. Geosci. Remote Sensing*, vol. 30, pp. 276–292, 1992.
[44] J. C. Eidenshink and J. L. Faundeen, "The 1 km AVHRR global land data set: first stages in implementation," *Int. J. Remote Sensing* vol. 15, pp 3443–3462, 1994.

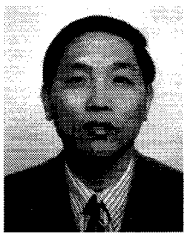

Zhanqing Li received the B.Sc. and M.Sc. degrees in climatology from Nanjing Institute of Meteorology, Nanjing, P.R. China, and the Ph.D. degree in satellite meteorology from McGill University, Montreal, Que., Canada, in 1983, 1986, and 1991, respectively.

He spent one year at the Atmospheric Environment Services of Canada as a NSERC Visiting Scientist. Since 1992, he has been a Research Scientist at the Canada Centre for Remote Sensing, Ottawa, ON. He has had over 30 journal articles published. Currently, he leads several research projects concerning the Earth's radiation budgets and climate, remote sensing of terrestrial parameters, correction of artifacts in satellite measurements, and space-borne fire monitoring.

Josef Cihlar received the B.Sc. degree in agricultural engineering from the University of Agriculture, Prague, Czechoslovakia, in 1967, the M.Sc. degree in soil science from the University of Guelph, Guelph, Ont., Canada, in 1971, and the Ph.D. degree in geography and remote sensing, from the Univerity of Kansas, Lawrence, KS, in 1975.

Between 1975 and 1991, he worked as a Scientist and Head of the Applications Development Section at the Canada Centre for Remote Sensing (CCRS), Ottawa, ON. Presently, he is a Research Scientist and Head of the CCRS Environment Monitoring Section. His research interest is on the use of satellite observations for monitoring and modeling environmental change over land at regional to continental scales. He is involved in several interdisciplinary projects, including the boreal ecosystem-atmosphere study (BOREAS) and the northern biosphere observation and modeling experiment (NBIOME).

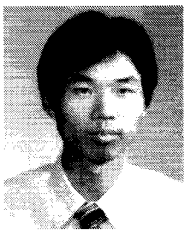

Xingnian Zheng was born in 1962. He received the B.Sc. and M.Sc. degrees from Nanjing University, Nanjing, P.R. China, in 1984 and 1987, respectively.

Currently, he is an Associate Professor at the Institute of Remote Sensing Applications, Chinese Academy of Sciences, Beijing, P.R. China. In 1995, he worked at the Canada Centre for Remote Sensing, Ottawa, ON, as a Visiting Scholar. He has had more than 40 articles, books, and maps published. His main research interests include remote sensing, geographical information system (GIS), and modeling, as well as their applications to resources and the environment.

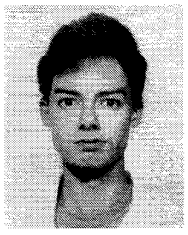

Louis Moreau received the B.Sc. degree in physics from Laval University, Quebec City, Canada, and the M.Sc. degree in atmospheric and oceanic sciences from McGill University, Montreal, Quebec, Canada, in 1991 and 1993, respectively.

After 1993, he joined Intermap Information Technologies Ltd. (formerly known as Intera), Ottawa, Canada. He has worked on projects related the photosynthetically active radiation, radiation modeling, and detection of forest fires at the Canada Centre for Remote Sensing, Ottawa, ON, Canada.

Hung Ly, photograph and biography not available at the time of publication.